Biosensors and Bioelectronics 47 (2013) 329–334

Contents lists available at SciVerse ScienceDirect

Biosensors and Bioelectronics

journal homepage: www.elsevier.com/locate/bios

In-situ growth of micro-cubic Prussian blue–TiO_2 composite film as a highly sensitive H_2O_2 sensor by aerosol co-deposition approach

Zhenyu Chu, Lei Shi, Yu Liu, Wanqin Jin*, Nanping Xu

State Key Laboratory of Materials-Oriented Chemical Engineering, College of Chemistry and Chemical Engineering, Nanjing University of Technology, 5 Xinmofan Road, Nanjing 210009, PR China

ARTICLE INFO

Article history:
Received 29 January 2013
Received in revised form
4 March 2013
Accepted 4 March 2013
Available online 28 March 2013

Keywords:
In-situ growth
PB–TiO_2 composite film
Aerosol co-deposition
H_2O_2 sensor

ABSTRACT

Assisted by the aerosol co-deposition approach, Prussian blue (PB)–TiO_2 composite film can be *in-situ* formed in one step. The architecture of this film is constructed by two layers: PB–TiO_2 nano-particles as a ground layer and individual PB micro-cubes as a top layer. Together with the strong electrocatalytic ability from regular PB morphology, TiO_2 can denote its high catalysis in H_2O_2 detection attributed by the extinction of band gap since the combination of PB. Under a low operation potential –0.05 V, this sensor exhibits an ultrasensitive ability (1726.8 μA mM^{-1} cm^{-2}), stability and low detection limit (1.5 μM) in H_2O_2 analysis. The application of this composite material is hopeful to extend in complex physiological analysis, and the preparation approach is promising to extend in more composite materials *in-situ* synthesis.

1. Introduction

The purpose of biosensor research is continuously enhancing performance in order to satisfy humans' various demands, such as food and production safety (Raz et al., 2010), clinic treatment (Xu et al., 2010), disease control (Lu et al., 2007). Among lots of physiological activators, hydrogen peroxide (H_2O_2) is an essential detection target which refers to nearly all application fields. In some situation, H_2O_2 is able to provide the positive power (Villegas et al., 2005; Tan et al., 2012), but sometimes, it will be harmful to our body or health (Kitsati et al., 2012; Silva et al., 2012). Accordingly, the improvement of accuracy and sensitivity in H_2O_2 detection is still attracting many attentions from scientists. Characters of modified material are normally crucial to the performance of biosensors. Hence, in order to realize both high performances in sensitivity and accuracy, material selection should be well considered.

Owing to the low detection potential and good electrocatalytic ability to H_2O_2, Prussian blue (PB) is widely called "artificial peroxidase" (Karyakin et al., 2000; Lu et al., 2006). In our previous work, we have focused on the morphology design and control of PB film. Relied on our developed preparation approaches, such as aerosol deposition (Chu et al., 2010), electric field induced self-assembly (Chu et al., 2011) and template hole fill-in method (Chu et al., 2012), PB has already formed various regular structures. However, although original property of PB is very suitable to serve as a H_2O_2 sensing material, the further improvement is difficult due to its essence limitation. Generally, in order to enhance the performance of one material, another active substance can be doped for assistance (Stankovich et al., 2006; Galan-Vidal et al., 1998). If a high catalytic material can be compatible with PB film, meanwhile the formed film also realizes a regular morphology, the performance can be expected to improve. TiO_2 is a nontoxic oxide with the high catalysis, stability and biocompatibility (Wang et al., 2010). Its application has already referred to biosensor fabrication, but requiring a high detection potential (Cosnier et al., 1997; Cao et al., 2008). This could cause an evident interference from other co-existed compounds in real detection system. While, PB can erase above defects because of its potential reduction function. Thereby, combination of PB and TiO_2 will be desired to possess both high catalysis from TiO_2 and excellent anti-interference from PB. However, with the existence of TiO_2, *in-situ* regular growth of PB is not easy to realize due to the disturbance of assembly and crystallization space.

In this work, we designed to apply aerosols as the reactive unit for co-deposition of TiO_2 and PB because of their small volume and uniform distribution. These properties can separate and decrease the adverse effects of TiO_2 for regular PB crystallization. In one step, uniform PB micro-cubes can be *in-situ* formed on a layer of PB–TiO_2 composite ground film. According to the performance characterizations, the introduction of TiO_2 can reduce 50% of PB surface concentration, but harvesting ca. 50% sensitivity increase in H_2O_2 detection. Moreover, enhancement mechanism is further confirmed that this composition can obviously decrease the band

* Corresponding author. Tel.: +86 25 8317 2266; fax: +86 25 8317 2292.
E-mail address: wqjin@njut.edu.cn (W. Jin).

0956-5663/$ - see front matter © 2013 Elsevier B.V. All rights reserved.
http://dx.doi.org/10.1016/j.bios.2013.03.023

gap of TiO_2 to arouse its catalytic function, and regular cubic shape is able to intensify the electrocatalysis of PB film.

2. Experimental section

2.1. Reagents and apparatus

$K_4[Fe(CN)_6]\cdot 3H_2O$ (Sigma-Aldrich), $FeCl_3\cdot 6H_2O$ (Sigma-Aldrich), Ascorbic acid (Sigma-Aldrich), Uric acid (Sigma-Aldrich) and 30 wt% H_2O_2 (Sinopharm Chemical Reagent Co., Ltd, China) were of analytical grade purity and used without further purification. TiO_2 powder (P25, 80% anatase, 20% rutile) was purchased from Degussa with average size of 21 nm. All solutions were prepared with deionized water.

The electrochemical properties were characterized by electrochemical workstation (CHI 660C, (Shanghai Chenhua, China). All cyclic voltammetry (CV) were operated in 0.05 M phosphate buffer (pH=6.5) with 0.1 M KCl at 25 °C. Pt wire and Ag/AgCl were served as the counter and reference electrodes, respectively. Scanning rate was kept 50 mV/s. Field emission scanning electron microscopy (FESEM) (Hitachi-4800, Japan) characterization were operated to investigate the film morphologies. The spectral properties were studied by UV–vis spectroscopy (PerkinElmer lambda 950, USA). XRD patterns were taken by X-ray diffractometer (Miniflex 600, Japan). Raman spectrum was characterized by Raman spectrometer (Horiba Labram HR 800, Japan).

2.2. Pretreatment of Pt electrode

In order to keep the electrode clean, pretreatment was used on the platinum foil surface ($7\times 2\ mm^2$). The surface of Pt electrode was first polished as mirror using metallographical sand paper, and then dipped into the Piranha solution (7:3 mixture of H_2SO_4/H_2O_2, v/v) for 30 min and rinsed with water. After ultrasonic washing in water for 30 min, the Pt electrode was ready for use.

2.3. Growth of PB film

For the deposition of PB films, two solutions were prepared. Solution 1: 0.01 M $K_4[Fe(CN)_6]$+0.1 M KCl+0.1 M HCl. Solution 2: 0.01 M $FeCl_3$+0.1 M KCl+0.1 M HCl+0.02 g TiO_2. The concentrations of reactive solutions were kept the same as our previous work for comparison (Chu et al., 2010). The adsorption of $K_4[Fe(CN)_6]$ is the most important step for the aerosol deposition approach. Accordingly, in order to protect the freshness of reactive $K_4[Fe(CN)_6]$ and PB formation, we only added TiO_2 powder into $FeCl_3$ solution. The prepared $K_4[Fe(CN)_6]$ solution and $TiO_2/FeCl_3$ suspension were respectively filled in two ultrasonic nebulizers (Shanghai Yu Yue Medical Equipment Co., Ltd, China; Size: $240\times 130\times 200\ mm^3$; Power: 50 W; Frequency: 1.7 MHz). As shown in Fig. S1, a Pt electrode was first fixed in one airtight organic glass container. Then, $K_4[Fe(CN)_6]$ aerosol was continuously injected into the container for certain hours. The average injection rate is 1.5 mL min^{-1}. Subsequently, $TiO_2/FeCl_3$ aerosol was injected for the same time after the former aerosol exhausted. The following description of deposition time is the total time of $K_4[Fe(CN)_6]$ and $TiO_2/FeCl_3$ deposition periods. The prepared electrodes were cleaned with deionized water and heated at 100 °C for 1 h to dehydrate.

2.4. Density functional theory (DFT) simulation

All the simulative processes were set at the level of DFT by Cambridge sequential total energy package (CASTEP). The Perdew–Burke–Ernzerhof functional (PBE) of gradient-corrected functional was chosen as the exchange-correlation functional. Ultrasoft pseudopotential was chosen to allow the calculation to run with the lowest possible cutoff energy for basis set. The electronic wavefunctions at each *k*-point were expanded in a plane-wave basis set up to 300 eV. The Monkhorst–Pack *k*-points for the accuracy of the Brillouin zone sampling were set at fine level. The SCF tolerance reached 1×10^{-6} eV/atom.

3. Results and discussion

3.1. Influence of deposition time

Prussian blue owns different valences of irons (Fe^{2+}, Fe^{3+}) in its unit cell. Imposing certain potentials can push its electron transfer to realize substance transformation. According to the change amount of electric quantity, the surface concentration of PB on electrode can be calculated. Deposition time is usually essential for the control of formation amount (Taberna et al., 2006; Strohm and Lobmann, 2005). Hence, focusing on different deposition times, CV technology was applied to characterize the sample PB electrodes which are prepared by 5, 6, 7, and 8 h, respectively. From the results of Fig. 1a, we can find that at the ranges of 0.15–0.19 V and 0.23–0.26 V, there are two obvious current peaks. These double peaks reveal the shift processes between Prussian blue ($Fe_2[Fe$

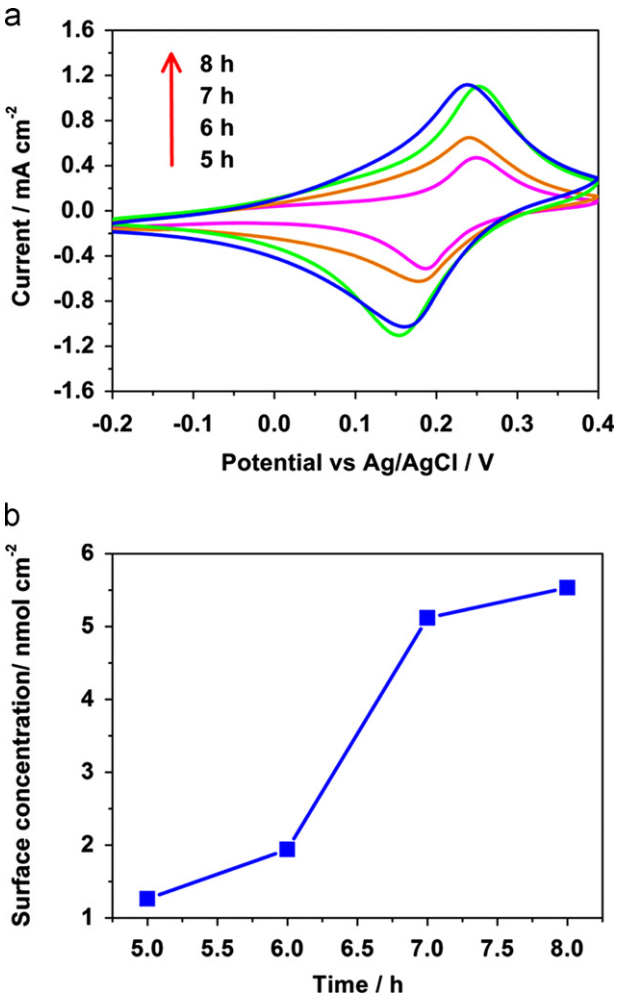

Fig. 1. (a) CV diagram of PB–TiO_2 modified electrodes which were prepared at 35 °C and in 5, 6, 7, and 8 h, respectively; and (b) diagram of calculated PB surface concentrations according to CV results.

$(CN)_6]_3$) and Prussian white ($Fe[Fe(CN)_6]$) caused by electron transfer. Therefore, higher current peaks can be judged to represent more PB amount. The exact values of PB surface concentrations Γ_T were calculated as following equation:

$$\Gamma_T = \frac{Q}{nFA} \quad (1)$$

where Q is the single peak area; A is the Pt electrode area; F is the Faraday constant; and n is the average electrons transfer which was calculated by $57/\Delta E$ (ΔE is the potential difference value between redox peaks).

The surface concentrations of PB which were prepared in 5, 6, 7, and 8 h were 1.264, 1.94, 5.118, and 5.5326 nmol/cm^2, respectively (Fig. 1b). At the beginning of deposition process (5–6 h), the formation rate of PB was very slow due to the time consumption of crystal nucleus growth on bare electrode surface. While after 6 h, PB can reach a rapid growth step based on already formed nucleus layer. But further increasing the deposition period, the increase of PB amount was again slow. That could be due to the nearly saturated electrode surface for PB loading. According to the CV diagram, ΔE of redox peaks were 0.062, 0.067, 0.080, and 0.103 V for 5, 6, 7, and 8 h, respectively. The potential difference of redox peaks also increases with time which illustrates the increase of electron transfer resistance. It is because TiO_2 itself is a bad conductor. Under the common conditions, electrons can hardly move through its body. With the continuous injection of TiO_2/$FeCl_3$ aerosol, more and more TiO_2 particles are adsorbed on electrode surface. Consequently, the existence of TiO_2 disturbed the original electron movement pathway to impel electrons across the location of TiO_2. In this case, the lengthened distance of electron transport will lead to the resistance increase.

Regular crystal shapes, especially in nano- or micro-scale, have been already confirmed to own outstanding abilities of catalytic activity, large contact area and rapid electron transfer rate (Kim and Cho, 2009; Carrara et al., 2008; Gu and Wong, 2006; Michel et al., 2007). Originally, $K_4[Fe(CN)_6]$ and $FeCl_3$ solutions will immediately react to form PB once they meet together. Aerosol deposition approach acquires more hours to form a PB film on electrode. This slow formation rate can often promote the sufficient crystallization. According to Fig. 2a and b, some cubic crystals are observed on film surfaces both for 6 and 8 h preparations. However, after 6 h growth, the ground film is not uniform. Some deficiencies caused the discontinuous film surface. Also, from digital photo (the inset of Fig. 2a), just partial electrode surface was covered by blue. This state changed if we increased the time to 8 h. More cubes with ca. 1 μm size have formed, and above deficiencies have been eliminated to exhibit an integrated film surface.

We selected one cube as the scanning region for EDX characterization. The results of energy spectrum (Fig. 2d) shows nonexistence of Ti element peaks, but the C, N, Fe elements of PB can be detected. This can illustrate the cubes were only consisted by PB crystallization. However, according to the XRD and Raman spectrum characterizations (Fig. S3 and S4), the characteristic peaks of TiO_2, anatase-type and rutile-type, can be both detected. Meanwhile, the intensities of PB peaks are not obviously decreased since the introduction of TiO_2. These evidences illustrate that TiO_2 (P25) was successfully doped into PB film without destruction of PB structure. We noticed that the ground film was composited by lots of round particles (Fig. 2c). This feature was due to the aggregation of PB and TiO_2 (Szacilowski et al., 2006). It is quite different with the only PB modified electrode also prepared by aerosol deposition approach (Fig. S2). Without introduction of TiO_2, the whole film surface was decorated by lots of regular edges which come from imperfect PB crystals. Here, because TiO_2 powder is heavy to precipitate and able to assemble PB crystals, larger size of round PB–TiO_2 particles will be produced as the ground film. Moreover, the distribution of cubes is more

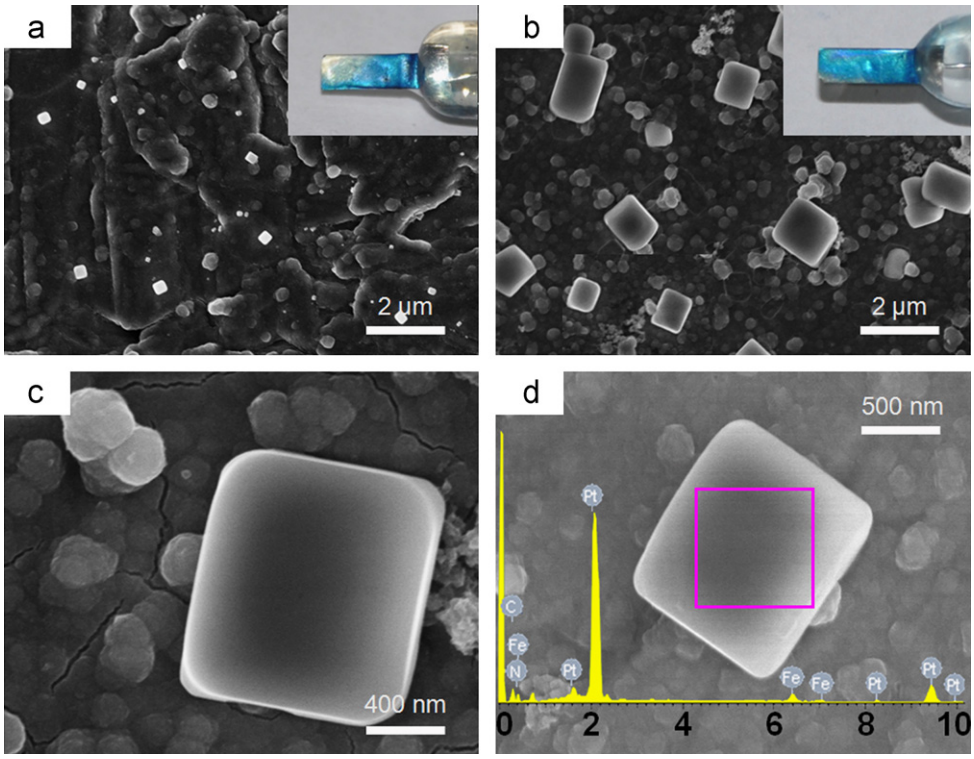

Fig. 2. FESEM images of PB–TiO_2 modified electrodes which were prepared at 35 °C and (a) 6 h, (b) 8 h. The insets of (a) and (b) are digital photos of PB electrode surfaces; (c) is the magnified morphology of (b). (d) EDX characterization result of the prepared PB–TiO_2 film. The pink box shows the selected scanning area. (For interpretation of references to color in this figure legend, the reader is referred to the web version of this article.)

separate as many islands. Isolate crystal distribution is benefited to increase the electrocatalysis and contact area of solution to treat as the collection of micro-electrodes (Karyakin et al., 2007). Each cube owns perfect edges which is the best catalytic sites for H_2O_2 reaction. Hence, by consideration of above results, the deposition time of 8 h can be applied as an appropriate condition for the fabrication of PB–TiO_2 composite film.

3.2. Influence of deposition temperature

In our previous work (Chu et al., 2010), 35 °C was confirmed the best deposition temperature for PB formation by aerosol deposition. But, it should be clear whether the existence of TiO_2 will affect the temperature of PB crystallization. Accordingly, PB sample electrodes were therefore respectively prepared at 30, 35, 40 °C for investigation. Surely, all the PB films were kept for 8 h deposition. CV scanning was again applied to investigate the PB amount on Pt electrode (Fig. 3). We found that, under 35 °C, the current peaks were higher than other two conditions, and the potential difference values were also larger. This may be due to the slight increase of electron transfer caused by thicker PB layer. Likewise, the surface concentrations of PB films were calculated as 3.866, 5.5326, and 3.976 nmol/cm^2 for 30, 35, and 40 °C by Eq. (1). The amount of PB prepared at 35 °C is nearly 1/3 enhancement than others. In this case, the morphology could change with different temperatures.

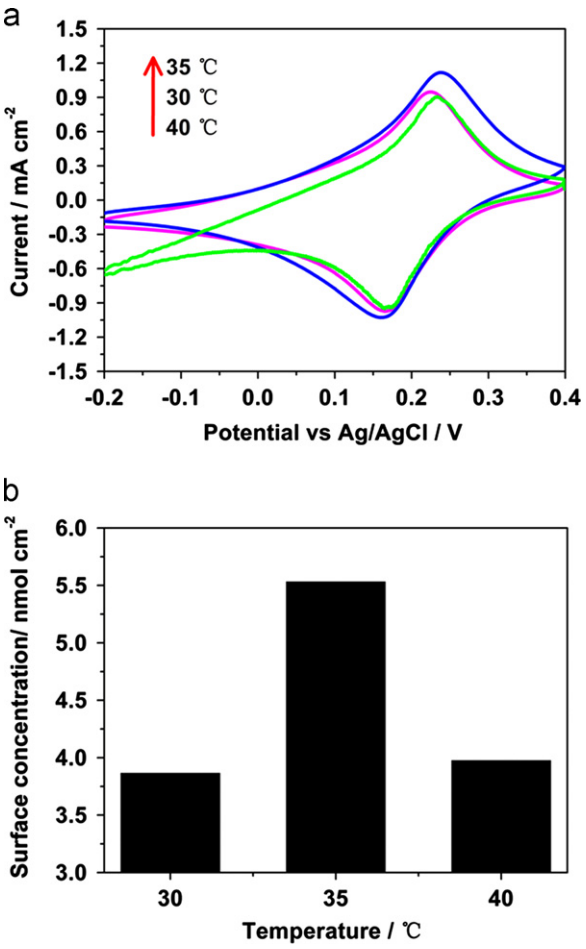

Fig. 3. (a) CV diagram of the prepared sample electrodes prepared in 8 h and at 30, 35, 40 °C, respectively; and (b) the calculated PB surface concentrations according to CV results.

The results show that (Fig. S5), only under 35 °C, cubic crystals appeared on electrode surface. Lower temperature may not provide enough thermal motion energy for the adsorption of reactive molecules which leads to the lower formation rate of PB amount. Therefore, on the ground film, just occurring the aggregation of crystals but not forming any regular structure due to the insufficient supplement of crystallization source. But over-high temperature will also hinder the morphology formation. We have confirmed that the adsorption of PB on Pt electrode is relied on Van der Waals force between $K_4[Fe(CN)_6]$ and Pt which is very weak in bonding (Chu et al., 2009). Higher temperature may cause a stronger molecular motion to push the escape of $K_4[Fe(CN)_6]$ from electrode surface. Furthermore, the whole film also presents lots of cracks due to the mismatch of thermal expansion. Accordingly, we select 35 °C as the optimized preparation temperature.

3.3. Performance characterization of H_2O_2 detection

We have already confirmed that 35 °C and 8 h are the optimum parameters for preparing the PB–TiO_2 composite film. In our purpose, we expected that TiO_2 can play its catalytic role to improve the performance of the as-prepared sensor. Thus, chronoamperometry experiment was applied to investigate whether TiO_2 will donate its catalysis function. During the test process, at each time intervals, we added the same concentration of H_2O_2 (10 μM) into buffer solution. The current response can be applied

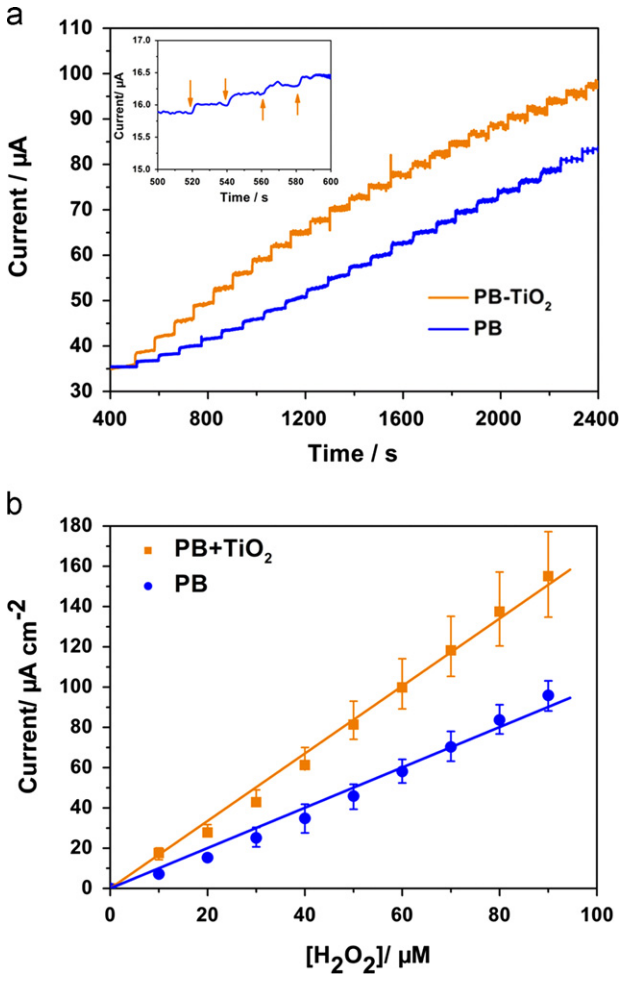

Fig. 4. (a) Chronoamperometry diagram of the prepared PB–TiO_2 film and PB film modified sensors. The inset is the testing diagram of detection limit, each arrow represents each addition of 1.5 μM H_2O_2; (b) the fitted linear of current response *vs.* H_2O_2 concentration according to the data of chronoamperometry results.

to judge the sensitive ability. After adding more than 20 times (Fig. 4a), the current step can also keep stable and distinct. This illustrates that the combination of TiO_2 will not affect the original stability of PB in H_2O_2 detection.

In order to obtain the detection limit of the prepared film, we continuously decrease the added H_2O_2 concentration. The least distinct amount is 1.5 μM. When this concentration was mixed into the buffer solution for several times, there are still current steps for each addition (the inset of Fig. 4a). Based on the chronoamperometry data, we fitted the diagram of current response vs. H_2O_2 concentration. The sensitivity was calculated as 1726.8 μA mM^{-1} cm^{-2}, the relative standard deviations (RSD) is 8.6%. Compared with the electrode only modified by PB film (1163 μA mM^{-1} cm^{-2}, RSD is 4.7%), this sensitivity nearly increase 50%. Moreover, we also compared their CV diagrams (Fig. S6). The redox current peaks of PB–TiO_2 are obviously lower than those of PB film. According to the calculation, PB surface concentrations are 5.5326 and 9.55 nmol cm^{-2} for PB–TiO_2 and PB modified electrodes, respectively. This result shows that the introduction of TiO_2 powder into reactive aerosol will affect the formation of PB crystals, nearly 50% decrease. But, on the contrary, the sensitivity has increased 50%. This is mainly attributed to the catalysis function of TiO_2 and the advantaged surface morphology. The anti-interference ability is also important for the accuracy of sensor. In real detection system, ascorbic acid (AA) and uric acid are the most two common co-existence substances, and also easy to cause the interference signal. According to our detection (Fig. S7), the addition of AA and UA with same concentration of H_2O_2 cannot produce the obvious current change. This well anti-interference ability is mainly due to the low application potential of PB–TiO_2 to avoid the redox of AA and UA. Besides, after the first application, the PB–TiO_2 based sensor can still maintain the 88% sensitivity of the fresh by the 15 days storage (Fig. S8).

It should be noted that TiO_2 is usually functioned by the excitation of UV light. However, in the whole detection process, UV lamp source was never applied. In this case, some changes may have occurred to produce the electron transition under the visible light.

3.4. Catalytic mechanism of PB/TiO_2 composite film

The spectral behaviors of the prepared sensors were studied by UV–vis spectroscopy. According to the results (Fig. 5), the light responses are quite different since the combination of PB and TiO_2. As well-known, the catalytic function of TiO_2 is rare at the range of visible wavelength due to the weak energy for electron excitation. Therefore, our results show that between 410 and 620 nm no adsorption of light occurred by TiO_2. But, PB can be helpful to fill up this blank. After the combination of PB, from UV region to infrared region, PB–TiO_2 can absorb all the lights for electron transition. In order to confirm the change of band gap, the data were treated by the $(\alpha h\nu)^{1/2}$ *vs.* $h\nu$ function, which can be applied in the determination of material band gap. It is obvious that the powder of TiO_2 owns a wide energy gap of ca. 2.91 eV, however, there is no band gap for PB–TiO_2 composite film (Fig. S9).

With the purpose of explanation in theory, we applied Density Functional Theory (DFT) as a tool to simulate the structures of TiO_2 before and after the combination of PB. Because the amount of anatase structure is much more than rutile structure, anatase TiO_2 was served as a representative model for quantum simulation. Each established cell structures of TiO_2 and PB–TiO_2 were first optimized to realize the geometry stability and energy minimum. Then the properties were calculated according to the theoretical structures (Fig. S10). Band structures of unit cell can describe the distribution of valance and conduction bands. Normally, the energy difference between LUMO (Lowest Unoccupied Molecular Orbital) and HOMO (Highest Occupied Molecular Orbital) is called energy gap. Higher value of energy gap illustrates the electron excitation acquires more energy to cross the gap for arriving the conduction band, thus this material behavior is more like an insulator (Brus, 1986; Chen et al., 2009). For TiO_2 structure, Fermi level locates at the HOMO and there is a wide blank without any band between ca. 0 and 2.5 eV (Fig. 6a). The band gap was calculated as 2.44 eV. This value is very close to our experimental data, 2.91 eV. Due to the lager gap than most of semi-conductors, commonly, TiO_2 can arouse its catalytic function only under UV light to excite valance electrons transition. However, once PB was

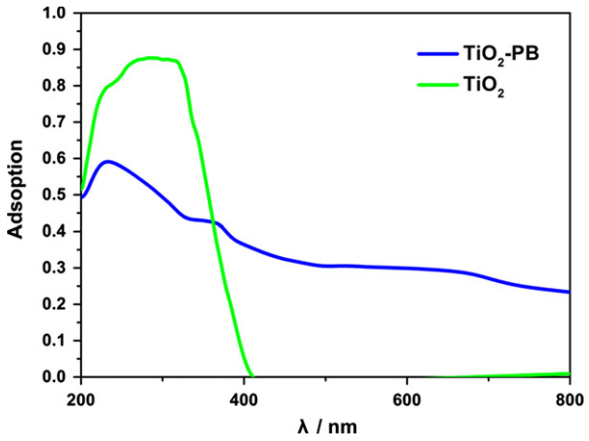

Fig. 5. Diffuse reflectance spectra of the prepared PB–TiO_2 composited film and TiO_2 powder.

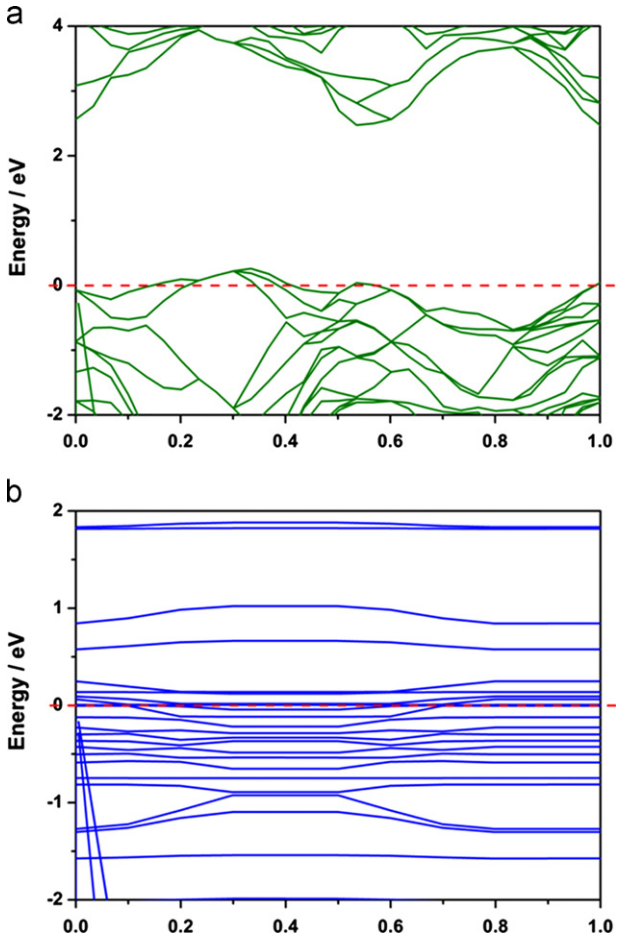

Fig. 6. The simulative band structures of (a) anatase TiO_2 and (c) PB–TiO_2 composited film. Fermi level was set to 0 eV, which is denoted by a red dashed line. (For interpretation of references to color in this figure legend, the reader is referred to the web version of this article.)

combined with TiO_2, the band structure has occurred obvious changes. The original band blank was filled by many new bands which attributed to the donation of PB bands (Fig. 6b). Moreover, around Fermi level, the distribution of bands is so tight that electrons can easily jump from HOMO to LUMO just with weak energy excitation. The bands of PB can be served as a "transfer station" to allow valance electrons of TiO_2 first jump to them, and then further bouncing to conduction band (Yamamoto et al., 2009). In this case, when we applied PB–TiO_2 composited film in H_2O_2 detection, under the natural visible light and impulse of potential, TiO_2 can donate its catalytic function in H_2O_2 detection. Meanwhile, because the regular cubes have separately distributed on the electrode, the whole film can provide many strong catalytic sites by their perfect edges as the collection of many independent micro-electrodes. This architecture is effective for the increase of the solution contact area and catalytic activity in H_2O_2 detection. Consequently, the excellent performance of PB–TiO_2 composited film can be ascribed to the synergistic effect of composition and micro-structure.

Furthermore, we also investigated the interaction between PB and TiO_2 to confirm the combination stability. Electron density was applied to judge the bonding possibility. As shown in Fig. S10, the green isosurface shows the electron movement area which can also be called electron cloud. If there forms a bond between two atoms, electrons can travel across the space between atoms which indicates the overlap of electron cloud (Wang, 2009). It is obvious that the oxygen atom from TiO_2 and iron atom from PB, titanium atom from TiO_2 and nitrogen atom from PB have all formed bonds. Further population calculation of these two bonds O–Fe and Ti–N exhibits that their lengths and populations are 1.84035 Å, 2.10643 Å and 0.13, 0.01, respectively. They are all standard ionic bonds which own strong interactions. In this case, the combination of PB and TiO_2 can keep strong stability. This is the reason that the current responses can still keep consistent since the repeated addition of H_2O_2.

4. Conclusions

We have successfully obtained the composite film of PB–TiO_2 by an aerosol co-deposition approach. This film was constructed by a PB–TiO_2 based ground layer and individual PB micro-cubes based top layer. Under the natural visible light and −0.05 V potential, the existence of TiO_2 can obviously increase 50% catalytic function to H_2O_2. The detection limit can reach 1.5 μm in H_2O_2 detection with good stability. The mechanism of excellent performance had further confirmed that the combination of PB and TiO_2 can extinct the wide band gap of TiO_2 to produce the possibility of electron excitation with visible light. The approach of aerosol co-deposition can extend current synthesis strategies of composite materials. This composite film can be expected to own wide application potentials in more fields, such as photovoltaic conversion, energy storage and physiological analysis.

Acknowledgment

This work was supported by the Doctoral Fund of Ministry of Education of China (20113221110001), the National Basic Research Program of China (No. 2009CB623406) and the National Natural Science Foundation of China (Nos. 20990222 and 21176115).

Appendix A. Supporting information

Supplementary data associated with this article can be found in the online version at http://dx.doi.org/10.1016/j.bios.2013.03.023.

References

Brus, L., 1986. Journal of Physical Chemistry 90, 2555–2560.
Cao, H., Zhu, Y., Tang, L., Yang, X., Li, C., 2008. Electroanalysis 20, 2223–2228.
Carrara, S., Shumyantseva, V., Archakov, A., Samori, B., 2008. Biosensors and Bioelectronics 24, 148–150.
Chen, Y., Analytis, J., Chu, J., Liu, Z., Mo, S., Qi, X., Zhang, H., Lu, D., Dai, X., Fang, Z., Zhang, S., Fisher, I., Hussain, Z., Shen, Z., 2009. Science 325, 178–181.
Chu, Z., Liu, Y., Jin, W., Xu, N., Tieke, B., 2009. Chemical Communications 24, 3566–3567.
Chu, Z., Zhang, Y., Dong, X., Jin, W., Xu, N., Tieke, B., 2010. Journal of Materials Chemistry 20, 7815–7820.
Chu, Z., Shi, L., Zhang, Y., Jin, W., Xu, N., 2011. Journal of Materials Chemistry 21, 11968–11972.
Chu, Z., Shi, L., Zhang, Y., Jin, W., Warren, S., Ward, D., Dempsey, E., 2012. Journal of Materials Chemistry 22, 14874–14879.
Cosnier, S., Gondran, C., Senillou, A., Gratzel, M., Vlachopoulos, N., 1997. Electroanalysis 9, 1387–1392.
Galan-Vidal, C.A., Munoz, J., Dominguez, C., Alegret, S., 1998. Sensors and Actuators, B 52, 257–263.
Gu, Y., Wong, W., 2006. Langmuir 22, 11447–11452.
Karyakin, A.A., Karyakina, E.E., Gorton, L., 2000. Analytical Chemistry 72, 1720–1723.
Karyakin, A., Puganova, E., Bolshakov, I., Karyakina, E., 2007. Angewandte Chemie International Edition 46, 7678–7680.
Kim, M., Cho, J., 2009. Advanced Functional Materials 19, 1497–1514.
Kitsati, N., Fokas, D., Ouzouni, M., Mantzaris, M., Barbouti, A., Galaris, D., 2012. Journal of Agricultural and Food Chemistry 60, 7873–7879.
Lu, D., Cagan, A., Munoz, R., Tangkuaram, T., Wang, J., 2006. Analyst 131, 1279–1281.
Lu, J., Drzal, L.T., Worden, R.M., 2007. Chemistry of Materials 19, 6240–6246.
Michel, M., Taylor, A., Sekol, R., Podsiadlo, P., Ho, P., Kotov, N., Thompson, L., 2007. Advanced Materials 19, 3859–3864.
Raz, S.R., Liu, H., Norde, W., Bremer, M., 2010. Analytical Chemistry 82, 8485–8491.
Silva, R., Montes, R., Richter, E., Munoz, R., 2012. Food Chemistry 133, 200–204.
Stankovich, S., Dikin, D., Dommett, G., Kohlhaas, K., Zimney, E., Stach, E., Piner, R., Nguyen, S., Ruoff, R., 2006. Nature 442, 282–286.
Strohm, H., Lobmann, P., 2005. Chemistry of Materials 17, 6772–6780.
Szacilowski, K., Macyk, W., Stochel, G., 2006. Journal of Materials Chemistry 16, 4603–4611.
Taberna, P.L., Mitra, S., Poizot, P., Simon, P., Tarascon, J.M., 2006. Nature Materials 5, 567–573.
Tan, J., Dong, C., Lu, Y.C., Xu, J.H., Luo, G.S., 2012. Industrial & Engineering Chemistry Research 51, 1834–1845.
Villegas, J.C., Garce, L.J., Gomez, S., Durand, J.P., Suib, S.L., 2005. Chemistry of Materials 17, 1910–1918.
Wang, Y., 2009. Journal of Physical Chemistry A 113, 10873–10879.
Wang, C., Yin, L., Zhang, L., Gao, R., 2010. Journal of Physical Chemistry C 114, 4408–4413.
Xu, S., Liu, Y., Wang, T., Li, J., 2010. Analytical Chemistry 82, 9566–9572.
Yamamoto, T., Saso, N., Umemura, Y., Einaga, Y., 2009. Journal of the American Chemical Society 131, 13196–13197.